UNIVERSAL WISER
PUBLISHER

Research Article

Enhancing Electrical Properties and Seebeck Effects of WO_3 Thin Films Using Spray Pyrolysis: Insights into the Conductivity and Carrier Type

Zahra Asghari[1*], Hamid Arian Zad[2] , Hosein Eshghi[1]

[1]Physics Department, Shahrood University of Technology, Shahrood, Iran
[2]Alikhanyan National Science Laboratory, Alikhanian Br. 2, 0036 Yerevan, Armenia
 E-mail: zahraasghary42@yahoo.com

Abstract: This study focuses on enhancing the electrical and thermoelectric properties of tungsten trioxide (WO_3) thin films using the spray pyrolysis technique. Three samples, namely A_1, A_2, and A_3, were prepared by depositing the films onto glass substrates at different deposition rates: R_1 = 1 mL/min, R_2 = 3 mL/min, and R_3 = 7 mL/min, respectively. Subsequently, the films underwent annealing at 500 °C for 2 hours in the air. A detailed investigation was conducted to analyze the structural, morphological, optical, and electrical properties of the WO_3 thin films. The Field Emission Scanning Electron Microscope (FE-SEM) images revealed the formation of circular strings with varying diameters for all layers. The diameter of each string decreased as the deposition rate increased. X-ray diffraction (XRD) structural analysis indicated that, before annealing, sample A_1 exhibited a polycrystalline nature with mixed tetragonal-hexagonal phases, while the other two samples were amorphous. After annealing, sample A_3 also became polycrystalline. Moreover, the UV-Vis spectra analysis demonstrated a monotonic decrease in the band gap of the layers with increasing spray rate, potentially attributed to the attenuation of the quantum confinement effect. The Seebeck effect was used to authenticate the n-type conductivity of the WO_3 layers, as the Seebeck effect and conductivity exhibited a direct connection. Furthermore, the current-voltage variation was found to align with the oxygen vacancies sites. Remarkably, the sample A_3 with the highest deposition rate exhibited the lowest resistivity.

Keywords: tungsten trioxide WO_3, seebeck effect, thermoelectrical properties

1. Introduction

Semiconductor characterization plays a crucial role in the advancement of semiconductor technology. Among the intermediate metal oxides, tungsten trioxide (WO_3) stands out as a widely studied *n*-type semiconductor with a large indirect band gap of approximately 2.4-3.7 eV [1-6]. Its optoelectronic properties have attracted considerable attention for potential applications such as smart windows [5-7], front contacts in photovoltaic solar cells [8-10], and variable-reflectance mirrors [11-12].

Thin films of WO_3 have recently gained significant prominence due to their excellent electrochemical stability, making them ideal for use as photo-anodes in photo-electrochemical cells [13-17]. There are other works that provide

insights into the fabrication techniques, properties, performance enhancement strategies, and potential applications of WO_3 thin films in the field of gas sensing [18-19]. Previous studies have reported the intrinsic reaction mechanism of WO_3/elaectrolyte interfaces in various electrolytes [20-23]. The deposition of WO_3 thin films has been achieved through various techniques, including physical vapor deposition (PVD), chemical vapor deposition (CVD) [24], evaporation [25-27], electrodeposition [28], sputtering [29-32], sol-gel deposition [27, 33], and spray pyrolysis technique [34-37]. The latter technique presents many advantages such as (i) short time deposition, (ii) simple technology, (iii) low-cost, (iv) no need for vacuum, and (v) large-scale area of thin film production.

Many researchers have devoted themselves to studying WO_3 thin films prepared under different spray rates [28] and the effect of annealing on the structural, surface morphological, and optical properties of WO_3 thin films [25, 29, 33, 38-39]. For example, the *p*-type conductivity of WO_3 thin films has been considerably investigated [24]. The materials were deposited by spray pyrolysis using a precursor tungsten hexachloride dissolved in ethanol. The authors of the same reference considered parameters such as deposition temperature and pressure of the carrier gas as typical variables, resulting in enhanced optical and electrical properties of the WO_3 thin films. The influences of deposition parameters on surface morphology, conductivity, and optical and electrochromic properties were studied using X-ray diffraction (XRD), current-voltage measurements ($I - V$), UV-Vis spectrometry, and other techniques [24].

The Seebeck effect, also known as the thermoelectric effect, is of great interest in semiconductor physics, as it allows for the determination of the type of dominating charge carriers in a material and the relative position of the Fermi level with respect to the transport level. Phenomenologically, the Seebeck effect can be understood as a temperature gradient-induced voltage generation due to the shift in the energetic distribution of free charge carriers in a metal or semiconductor. However, the investigation of the Seebeck effect in WO_3 has been relatively limited.

In this paper, we present a detailed investigation of the Seebeck effect in WO_3 thin films. Our study focuses on three different samples, examining the thermoelectrical properties of WO_3 and shedding light on the anomalous behavior of this fascinating material under different deposition rates and annealing conditions. We verify the influence of the deposition rate and annealing process on various physical properties of the WO_3 thin films, including conductivity, optical properties, and electrical behavior. Furthermore, we analyze the correlation between variations in the Seebeck effect and changes in the aforementioned properties across the different samples. Through this comprehensive analysis, we aim to gain a deeper understanding of the thermoelectrical properties of WO_3 and provide valuable insights into its potential applications [24-25, 28-29, 33, 38-39].

2. Experimental procedure: general information

The deposition of WO_3 thin films on glass substrates was carried out using the spray pyrolysis method. The precursor solution consisted of 50 mL of ammonium tungstate [$(NH_4)_2WO_4$], prepared by dissolving pure WO_3 powder (99.9%, Merck) in a mixture of ammonia and distilled water. Three different spray rates denoted as R_1 = 1 mL/min, R_2 = 3 mL/min, and R_3 = 7 mL/min, were used for the deposition. The other deposition parameters, including the spray solution volume, nozzle-to-substrate distance, and substrate temperature, were maintained at 50 mL, 30 cm, and 400 °C, respectively.

Prior to deposition, all substrates underwent a cleaning procedure. They were washed with soap and water, followed by immersion in a container containing acetone and distilled water. Subsequently, the substrates were placed in an ultrasonic machine for 16 minutes. Finally, the substrates were rinsed with deionized water and dried using nitrogen gas.

The preparation of transparent WO_3 thin films involved two steps. In the first step, a solution of ammonium tungstate [$(NH_4)_2WO_4$] was sprayed onto the preheated substrates (at 400 °C) using air as a gas conveyor. The experimental setup for the spray deposition process has been previously described in Ref. [40-42]. The resulting films exhibited transparency, amorphous structure, homogeneity, and good adhesion to the substrate. In the second step, the sprayed films were annealed in ambient air. The annealing temperature was fixed at 500 °C, and the annealing time was set to 2 hours. The annealed films appeared transparent with a slightly yellowish color. The deposition of the WO_3 thin layer followed the chemical reactions [43]:

$$(NH_4)_2WO_4 \xrightarrow{400\ °C} WO_3 + H_2O + 2NH_3 \qquad (1)$$
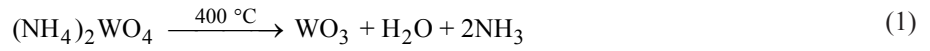
The morphologies of the samples were investigated using a Field Emission Scanning Electron Microscope (FE-SEM) (SIGMA 300-HV, Carl Zeiss). The structural characterization of the films was performed using X-ray diffraction (XRD) with CuK_α radiation (wavelength of 1.54 Å) and an angular range of 2θ from 10 to 70 degrees (XRD; Bruker AXS). The transmittance spectra of the studied samples were measured using a UV-Vis spectrophotometer (Shimadzu UV-Vis 1,800) in the wavelength range of 300-1100 nm. The film thickness was determined using a Taylor/Hobson profile meter with an accuracy of ± 20 nm.

3. Results and discussion

The Seebeck effect, also referred to as the thermoelectric effect, is a phenomenon that occurs when there is a temperature difference across a conductor, such as a metal or a semiconductor, resulting in the generation of an electric voltage. This effect is based on the behavior of charge carriers, such as electrons or holes, in response to temperature gradients. When a temperature gradient is applied to a conductor, meaning one end is heated while the other end is cooled, the charge carriers experience an imbalance in their distribution. Due to their thermal energy, the charge carriers diffuse from the hotter region to the colder region, seeking equilibrium. As a result, an accumulation of charge occurs at both ends of the conductor, creating an electric field. The electric field gives rise to a potential difference or voltage between the two ends of the conductor, which can be measured as the Seebeck voltage. This voltage is directly proportional to the temperature difference across the conductor. Hence, a larger temperature gradient will result in a higher Seebeck voltage. The Seebeck effect is fundamental to thermoelectric devices, which utilize this phenomenon to convert heat energy directly into electrical energy or vice versa. These devices, known as thermoelectric generators or thermoelectric coolers, find applications in various fields, including power generation, waste heat recovery, and temperature control systems.

Overall, the Seebeck effect demonstrates the conversion of a thermal gradient into an electric potential, highlighting the interconnected nature of temperature and electrical phenomena in conductive materials.

3.1 *Non-annealed characterization of the WO_3 layers*
3.1.1 *Surface morphology: FE-SEM analysis*

Figure 1 displays FE-SEM images of the grown samples A_1, A_2, and A_3 with their corresponding rates R_1, R_2, and R_3, captured at two scales: 20 µm and 5 µm. The FE-SEM images reveal that all samples are coated with numerous flat thin layers, forming spiral strings with rotating clusters known as lattice tungsten filaments. Notably, the presence of tungsten filaments with varying diameters is evident in all layers. The diameter of these filaments decreases with an increase in the deposition rate.
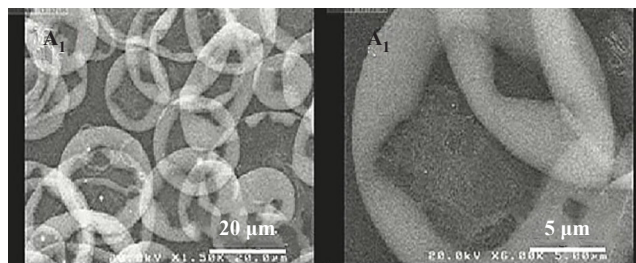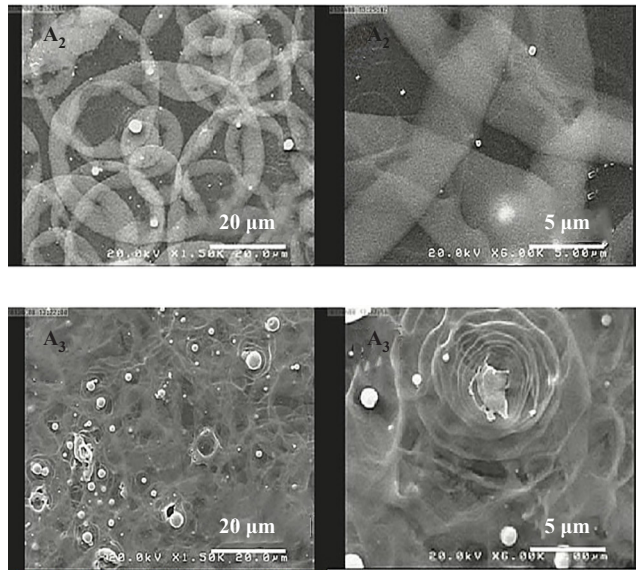
Figure 1. The FE-SEM images of the prepared WO_3 samples are shown at three different spray rates: $R_1 = 1$ mL/min, $R_2 = 3$ mL/min, and $R_3 = 7$ mL/min

3.1.2 *Structural properties*

The XRD patterns of the studied layers are shown in Figure 2. Upon inspecting this figure, it is evident that the sample with the lowest deposition rate, R_1, exhibits a polycrystalline nature. It consists of both tetragonal and hexagonal phases, with lattice parameters of $a = b = 23.33$ Å and $c = 3.79$ Å for the tetragonal phase, and $a = b = 7.29$ Å and $c = 3.89$ Å for the hexagonal phase. The patterns were indexed using SigmaPlot software, and it was observed that all peaks were in good agreement with the hexagonal structure of WO_3 by utilizing the standard data (JCPDS No. 05-0392) [44]. On the other hand, the samples grown at higher deposition rates, R_2 and R_3, appear to be in the amorphous phase. Using theoretical analysis associated with the crystalline structure, it is possible to deduce the distance between adjacent planes and the crystallite size in the grown samples. The distance between crystal planes, denoted as $d(hkl)$, can be obtained using Bragg's formula.

$$d(hkl) = \frac{n\lambda}{2\sin\theta} \tag{2}$$

Accordingly, the crystallite size corresponding to a given Bragg's angle θ can be found using Scherrer equation [45]

$$D = 0.9\frac{\lambda}{\beta\cos\theta} \tag{3}$$

where λ is the X-ray wavelength and β is the full width at half maximum (FWHM) of the given peak. By using Equation (3), for the (3 1 0) peak positioned at the Bragg's diffraction angle of $\theta \approx 12°$, the crystallite size of sample A_1 is estimated to be around 16 nm. Additionally, the dislocation density δ of the sample can be calculated using the formula $\delta = 1/D^2$ [46] (for more information, see Table 1).
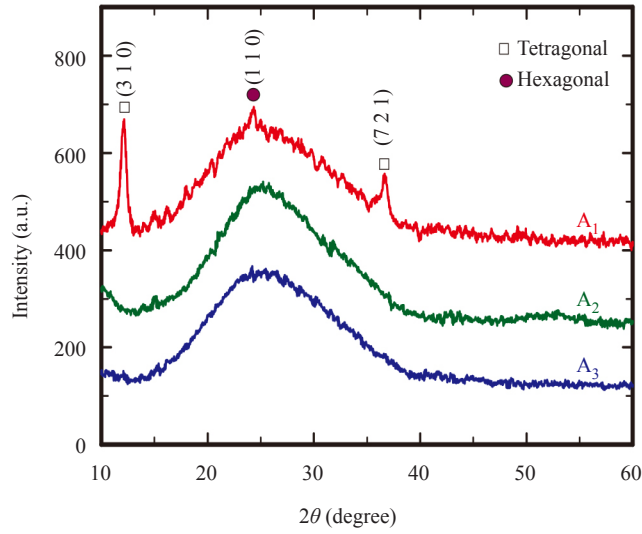
Figure 2. The XRD spectra of studied WO_3 thin layers. The sample A_1 possessing the lowest deposition rate R_1 has been grown with a polycrystalline nature in a mixed tetragonal and hexagonal phases. Other samples were grown in amorphous phase

Table 1. Crystallite size, distance between crystal planes, strain, and density of dislocations in sample A_1 were analyzed

Sample	D(nm)	d_{hkl}(nm)	$\varepsilon(\times 10^{-3})$	$\delta(\times 10^{-3})(nm)^{-2}$
A_1	15.93	0.733	2.17	3.9

3.1.3 *Electric and thermoelectric properties*

The measurement tool description of the Seebeck effect for electric and thermoelectric properties is given as follows. A metal-semiconductor connection can be established to investigate the conductivity of the sample using an electroaccumulation device. This device offers different modes, including Cyclic Voltammetry (CV), Structure Porous Carbon (CPC), Hydrothermal Carbon (CHC), and extra [47]. In our study, we specifically employed the CV mode. The device settings involve defining a potential range from E_1 to E_2 and determining the number of steps for this scanning process as well as the repetitions of this potential cycle. Subsequently, by connecting the electrical terminals of the device to the output terminals of the component and applying voltage within a specific range, we measure the current flowing through the sample.

Figure 3 illustrates the current voltage curves of the samples under investigation. The plots clearly demonstrate that all samples exhibit an ohmic behavior, and the resistivity of the layers decreases as the spray rate increases. To further elaborate on this phenomenon, we provide the following explanation. The sheet resistance, denoted as R_{sh}, can be determined by the ratio of voltage (V) to current (I), while the resistivity of the layers (ρ) is obtained from the relation $\rho = R_s t$, where t represents the thickness of the layer. In our measurements, these quantities were evaluated for a 1×1 cm^2 area of the samples. Figure 4 (a) displays the resistivity variations of the studied layers. The plot reveals a significant decrease in resistivity from 71.3 Ω·cm for R_1 to approximately 18.8 Ω·cm for R_3, which corresponds to the highest spray rate. This decrease in resistivity can be attributed to an increase in the density of oxygen vacancies within the network layer as the spray rate increases.
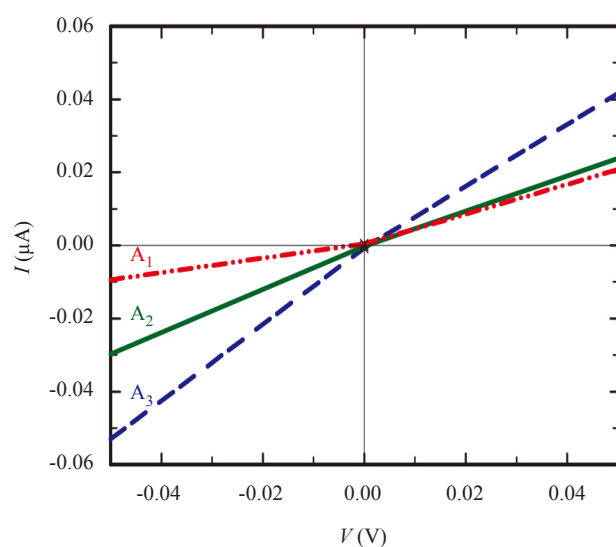
Figure 3. The $I - V$ curves of the three studied samples are depicted in Figure 3. The plots exhibit a clear ohmic behavior, indicating that the samples follow Ohm's law

To determine the type of conductivity (either n-type or p-type) exhibited by the samples, we employed the Seebeck effect relation $\mathcal{V} = S\Delta T$ [48], where S is the Seebeck coefficient, $\mathcal{V}$ is the thermoelectric power, and ΔT is the temperature difference across the width of the sample. The experimental results for the Seebeck effect are presented in Figure 4 (b).

Based on these results, it can be concluded that the Seebeck coefficient of the samples is negative, indicating n-type conductivity. Previous studies have reported an inverse proportionality between the Seebeck coefficient and the conductivity of the layer [49]. This finding is consistent with our obtained values from the $I - V$ data for the sheet resistance of the samples.
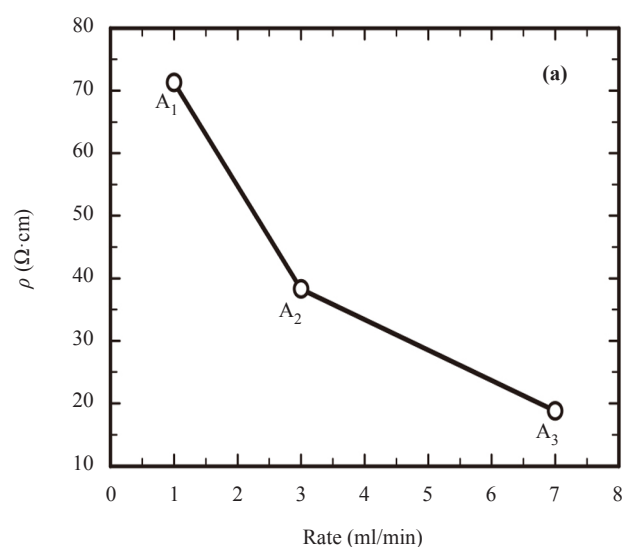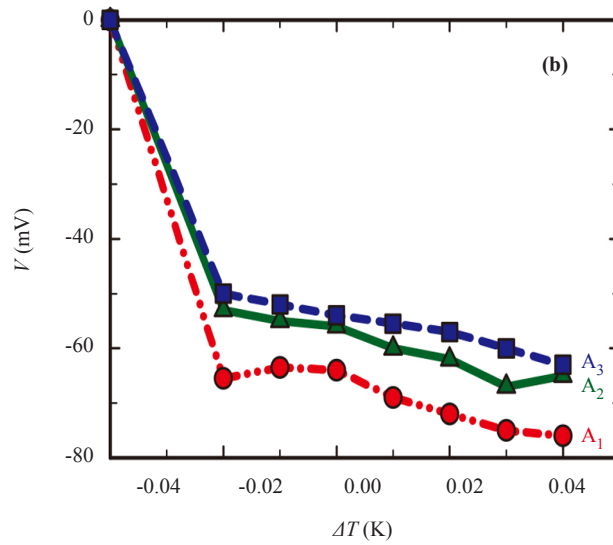
Figure 4. (a) The dependence of the electrical resistivity on the spray rate for the samples prepared using a subtractive process. The plot clearly shows a decrease in resistivity as the spray rate increases. This trend can be attributed to an increase in the density of oxygen vacancies within the network layer. (b) The experimental data of the Seebeck effect in the studied samples. The Seebeck coefficient, which is determined by the majority of carriers, indicates the type of conductivity exhibited by the samples. In this case, all layers exhibit n-type conductivity. The temperature difference across the width of the samples was fixed at $\Delta T = 1\,0\,°K$ during the measurements

3.1.4 *Optical properties*

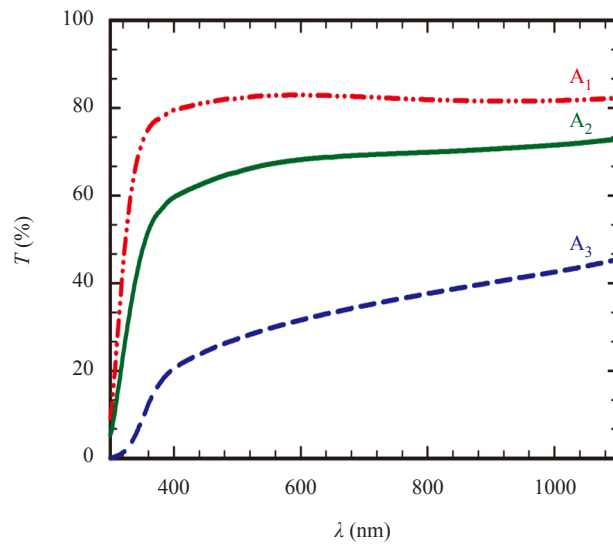**Figure 5.** The UV-Vis. transmittance spectra of the WO_3 films prepared under different spray rates ($1\ mL/min \leq R \leq 7\ mL/min$) are shown in Figure 5. The spectra illustrate the variation in transmittance across the UV and visible regions for the samples

Figure 5 displays the UV-Vis. transmittance spectra of the non-annealed samples. In the visible region (around $t \approx 550$ nm), the transmittance values are approximately 80% for A_1, 70% for A_2, and 30% for A_3. These variations in transmission are consistent with the improvement in the crystallinity of the layers and their thicknesses (approximately $t \approx 200 \pm 20$ nm, 235 ± 20 nm, and 290 ± 20 nm for the corresponding rates R_1, R_2, and R_3, respectively). The observed

changes in transmittance can be attributed to the reduction in photon scattering due to the better crystalline arrangement of the layers. As studied by M. Regragui et al. [34], the transmittance behavior is influenced by the annihilation of photon scattering, which is facilitated by the improved crystallinity in the layers. Consequently, we observe an enhancement in light transmission through the layers. Figure 6 depicts the spectra of the absorption coefficient of the samples as a function of wavelength λ, obtained using Lambert's equation.
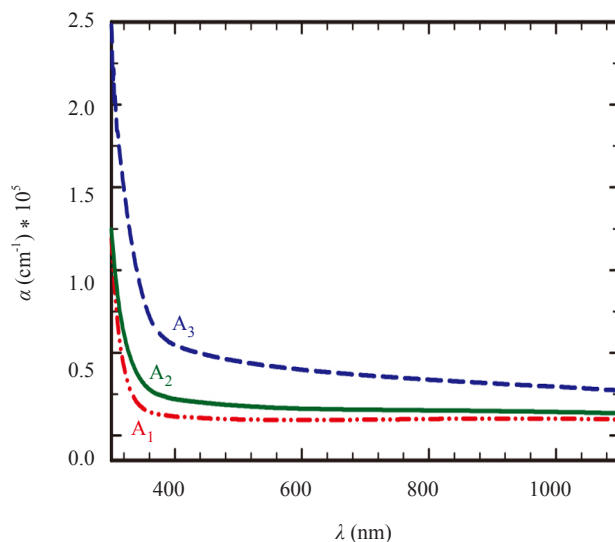

Figure 6. The absorption coefficient as a function of wavelength λ. In the ultraviolet region ($\lambda < 400$ nm), all samples exhibit high absorption coefficients, approximately on the order of 10^4 cm^{-1}

$$\alpha = -\frac{\ln T}{t} \qquad (4)$$

It is evident from this figure that all three samples exhibit relatively high absorption coefficients, approximately on the order of 10^4 cm^{-1}, in the ultraviolet region ($\lambda < 400$ nm). Consequently, sample A_1 grown at rate R_1 dis-plays a sharp absorption edge at 320 nm. As the spray rate increases, the absorption edge shifts towards longer wavelengths. By utilizing this information, we can determine the optical band gap E_g of the investigated films using the following formula [50]:

$$(\alpha h v)^m = A(h v - E_g) \qquad (5)$$

Here, A represents a constant, $h v$ denotes the incident photon energy, and m depends on the nature of the band transition ($m = 2$ for direct transitions and $m = 1/2$ for indirect ones). The determination of both direct and indirect band gaps involves extrapolating the linear portion of the curve to the energy axis, specifically $(\alpha h v)^m = 0$. The analysis for the indirect band gaps is illustrated in detail in Figure 7 (a), and the final results are presented in Figure 7 (b). We observed that E_g increases from 3.11 to 3.51 eV as the spray rate decreases. These variations can be explained by the width of the distribution of defect states (mainly oxygen vacancies) near the conduction or valence band edges.
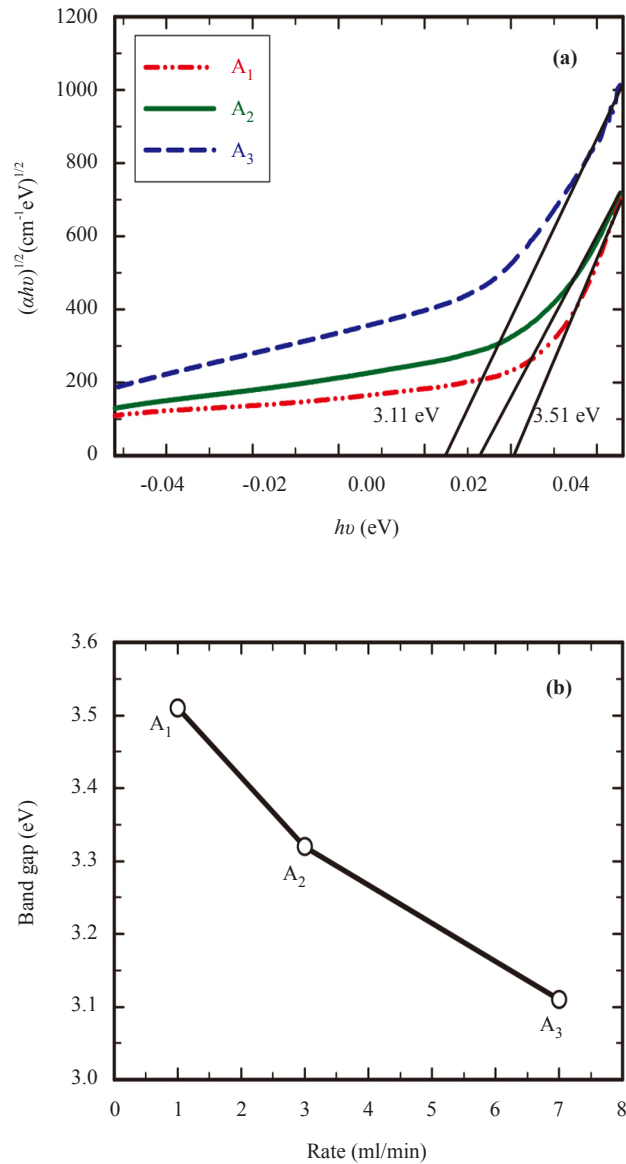
Figure 7. The details of the band gap determination: (a) indirect band gaps (b) The final calculated results and variations of E_g

3.2 *Annealed WO₃ layers characterization*

3.2.1 *Structural properties*

WO₃ thin films were deposited on glass substrates using the spray pyrolysis technique at three different rates: $R_1 = 1$ mL/min, $R_2 = 3$ mL/min, and $R_3 = 7$ mL/min. Subsequently, the films were annealed for 2 hours at 500 ℃ in air. XRD structural analysis revealed that the sample A_2 grown at a rate of $R_2 = 3$ mL/min exhibited an amorphous nature, while samples A_1 ($R_1 = 1$ mL/min) and A_3 ($R_3 = 7$ mL/min) were found to be polycrystalline. Figure 8 displays the crystalline structure of thin films after annealing. It is noteworthy that before annealing two samples with rates R_2 and R_3 had an amorphous nature, while the sample A_1 with rate R_1 had polycrystalline monoclinic structure. As shown in Figure 8 we see that after annealing samples A_1 and A_3 have polycrystalline structure, whereas the sample A_2 remains in the amorphous phase.

Interestingly, the sample A_1 is grown in three phases: monoclinic phase with lattice parameters $a = 14.49$Å, $b =$

14.50Å, c = 10.92Å, hexagonal phase with lattice parameters a = b = 7.28Å, c = 3.88Å and tetragonal phase with lattice parameters a = b = 7.56Å, c = 3.73Å. Moreover, A_3 sample is grown in the two aforedescribed phases: monoclinic with lattice parameters a = 14.49Å, b = 14.50Å, c = 10.92Å and hexagonal with lattice parameters a = b = 7.29Å, c = 3.89Å together with two new phases so-called ($5(NH_4)_2O \cdot 12WO_3$) and (($NH_4)_{0.42}WO_3$). The preferential directions for both polycrystalline samples are grown along (0 1 0) direction positioned at the Bragg angle of $\theta \approx 12°$ (JCPDS 05-0392). Other researchers have reported the same results for example in Refs. [24, 51].

Table 2. Crystallite size, distance between the crystal planes, strain and the density of dislocation of planes in the samples A_1 and A_3 after annealing

Sample	D(nm)	d_{hkl}(nm)	$\varepsilon(\times10^{-3})$	$\delta(\times10^{-3})(nm)^{-2}$
A_1	30.66	0.804	1.14	1.06
A_3	39.42	0.814	0.87	0.64

In order to further investigation of the obtained data, one can calculate crystal size, distance between network planes, strain and density of dislocation δ by implementing equations (2) and (3). Table 2 indicates that after annealing, the crystal size increases with an increase in the spray deposition rate, except for sample A_2 which remains in an amorphous phase. This phenomenon is consistent with the results reported in previous works [38, 52, 53]. It is worth noting that the distance between network planes is well-matched across the samples. It is interesting to mention that WO_3 exhibits unconventional behavior in the laboratory, and its structural properties studied by spray pyrolysis are unpredictable, resulting in either amorphous or crystalline structures. From the structural analysis results, we can calculate the strain $\varepsilon = \beta \cos(\theta)/4$ and the dislocation density $\delta = 1/D^2$ of the crystal plates [54]. The dislocation density represents the length of dislocation lines per unit volume of the crystal. Moreover, as the deposition rate increases, both the strain and the density of dislocations remarkably decrease, indicating improved crystallinity of the layers after annealing. This observation is consistent with the density of the (0 1 0) peak [38, 52].
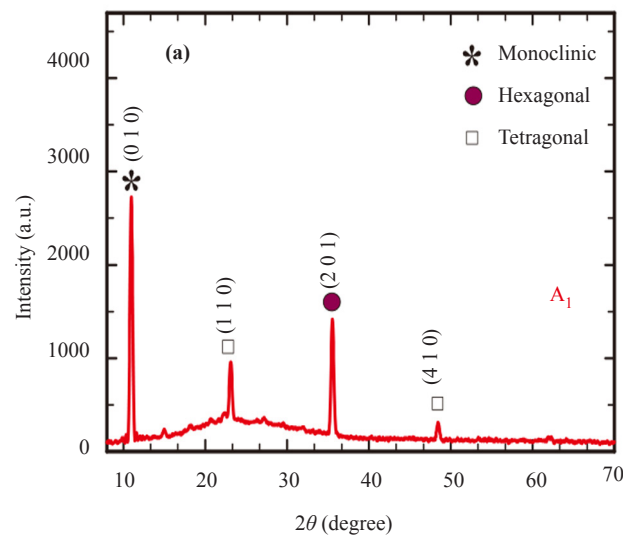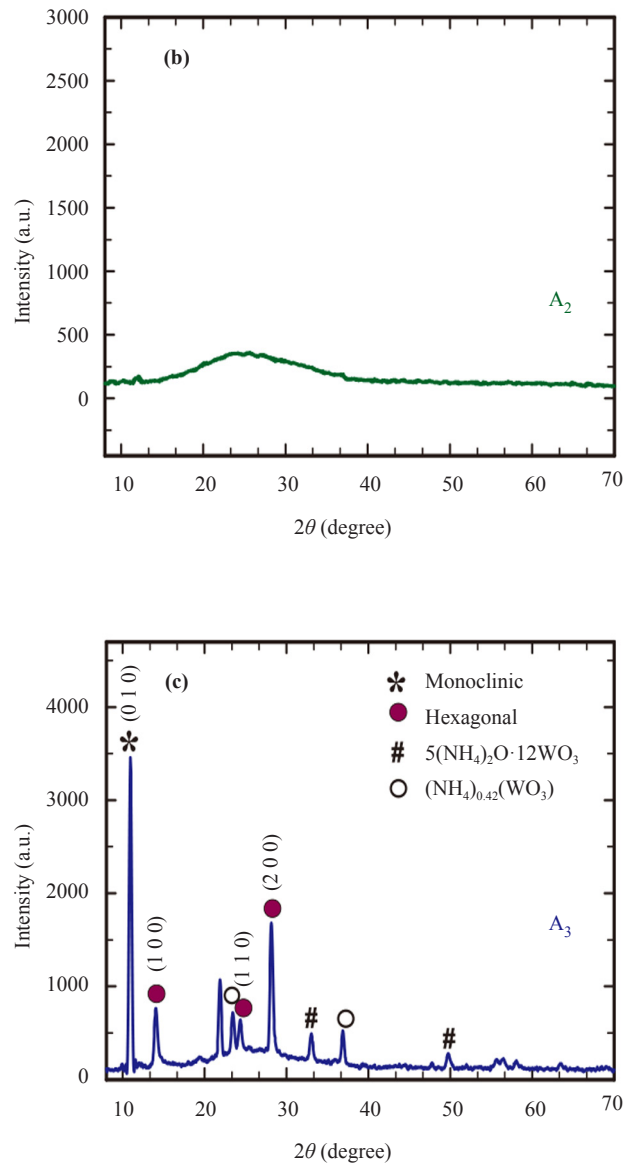
Figure 8. XRD diagrams of WO_3 thin layers prepared at TR = 400 °C and subsequently annealed at TA = 500 °C are shown in (a) A_1, (b) A_2, and (c) A_3. After annealing, A_1 and A_3 exhibit a polycrystalline structure, while A_2 remains in the amorphous phase

3.2.2 *Electrical and thermoelectric properties*

Figure 9 displays the $I − V$ curve of the studied samples after annealing. The sheet resistance R_{sh} of the layers decreases from 84 kΩ to 8.3 kΩ, indicating an improved electrical conductivity. Additionally, we observe a decrease in resistivity ρ from 1.9 Ω·cm to 0.26 Ω·cm, as shown in Figure 10 (a). The decrease in R_{sh} can be attributed to two reasons: firstly, the increase in carrier mobility, which depends on the dislocation density, and secondly, an increase in carrier density. The latter corresponds to an increase in acceptor concentration (tungsten vacancies/holes) relative to oxygen vacancies with an increase in both the spray deposition rate and annealing [34, 49, 55-57]. The experimental results for the Seebeck effect of the samples after annealing are presented in Figure 10 (b). The data clearly indicate that the majority of carriers in sample A_1 are electrons, indicating its *n*-type conductivity. On the other hand, samples A_2 and A_3 exhibit majority carriers as holes, indicating their *p*-type conductivity.

The observed conductivity types are a result of the deposition and annealing processes being performed in ambient air. During these processes, the surface of the WO$_3$ films can absorb oxygen, leading to the creation of tungsten vacancies with positive holes. The density of donor-like levels, particularly oxygen vacancies, decreases while the density of acceptor-like levels, specifically tungsten vacancies, increases. This phenomenon has been previously reported in the literature [58-59].

It is known that the *n*-type conductivity of WO$_3$ is primarily attributed to the presence of oxygen vacancies, which are associated with non-stoichiometry in the WO$_3$ lattice. The balance between the dopant concentration and oxygen deficit influences the *n*-type conductivity of the WO$_3$ layers. In our case, the deposition and annealing in an oxidizing environment (air) result in the reduction of oxygen vacancies during the annealing process. This reduction contributes to the generation of positive holes, leading to a switch from *n*-type conductivity to *p*-type conductivity.
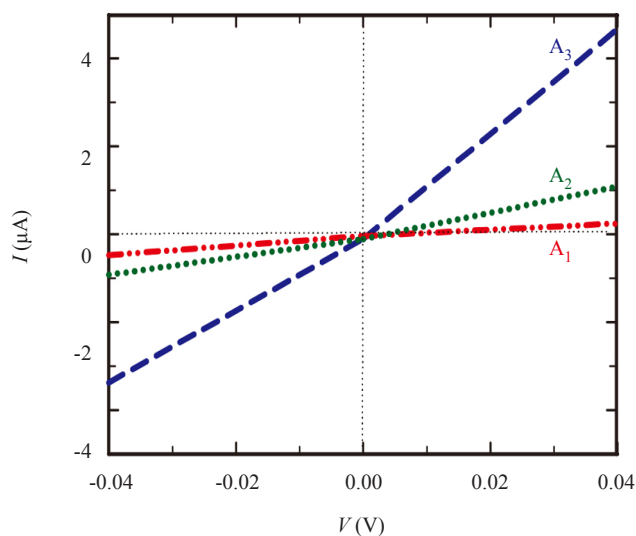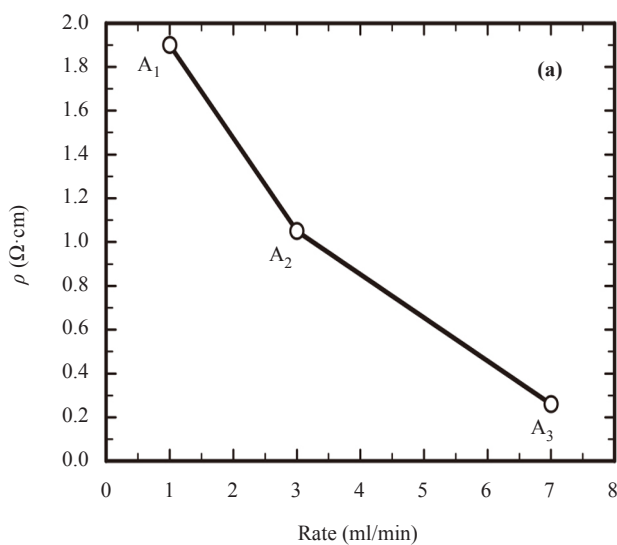

Figure 9. *I − V* characteristics of the studied samples after annealing. The plots exhibit clear Ohmic behavior, indicating a linear relationship between current and voltage for the samples
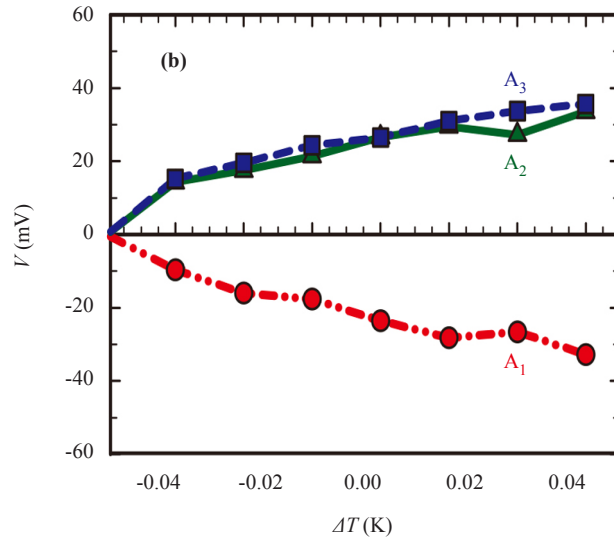
Figure 10. (a) Electrical resistivity of samples after annealing for 2 hours at 500 °C; (b) Experimental data of the Seebeck effect. The temperature difference $\Delta T = 10$ °C was maintained constant throughout the experiment

Furthermore, the highly oxidizing atmosphere can cause oxygen atoms to adsorb onto the surface of the WO_3 film, creating tungsten vacancies with six positive holes. This phenomenon is responsible for the *p*-type conductivity typically observed in WO_3 thin films [24].
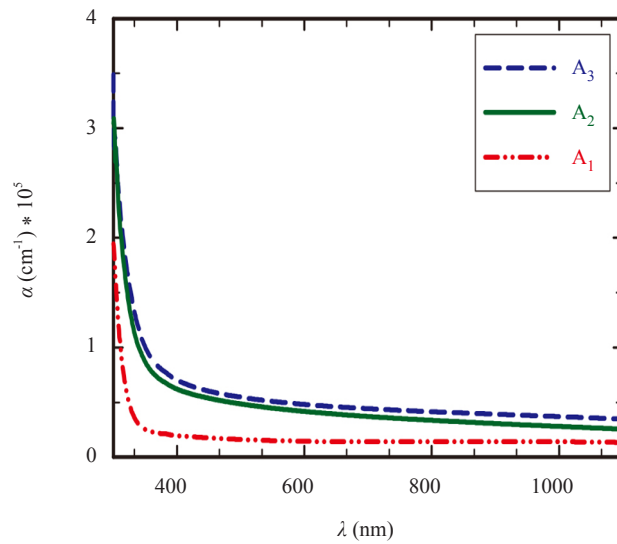
3.2.3 *Optical properties*

Figure 11. The variation of absorption versus wavelength

The optical properties of the annealed WO_3 thin films were extensively studied. After annealing, the absorption

coefficient (α) of the samples increases compared to the non-annealed stage. This indicates that the studied samples exhibit high absorbance properties ($\alpha \approx 10^5$ cm^{-1}) in the ultraviolet wavelength region ($\lambda \leq 400$ nm). Figure 11 illustrates the absorption as a function of wavelength (λ) for the annealed samples.

Using the absorption coefficient, we can straightforwardly determine the indirect optical band gap of the layers, as depicted in Figures 12 (a) and (b). From these figures, it can be observed that the band gap of the considered layers decreases from 2.77 eV in A_1 to 2.50 eV in A_3 as the spray deposition rate increases.

The quantum confinement effect (QCE) describes electrons in terms of energy levels, potential wells, electron energy band gaps, etc. It is observed when the size of the particle is too small to be comparable to the electron wavelength. WO_3 exhibits attractive properties due to the QCE caused by its small particle size (usually < 10 nm) [59].
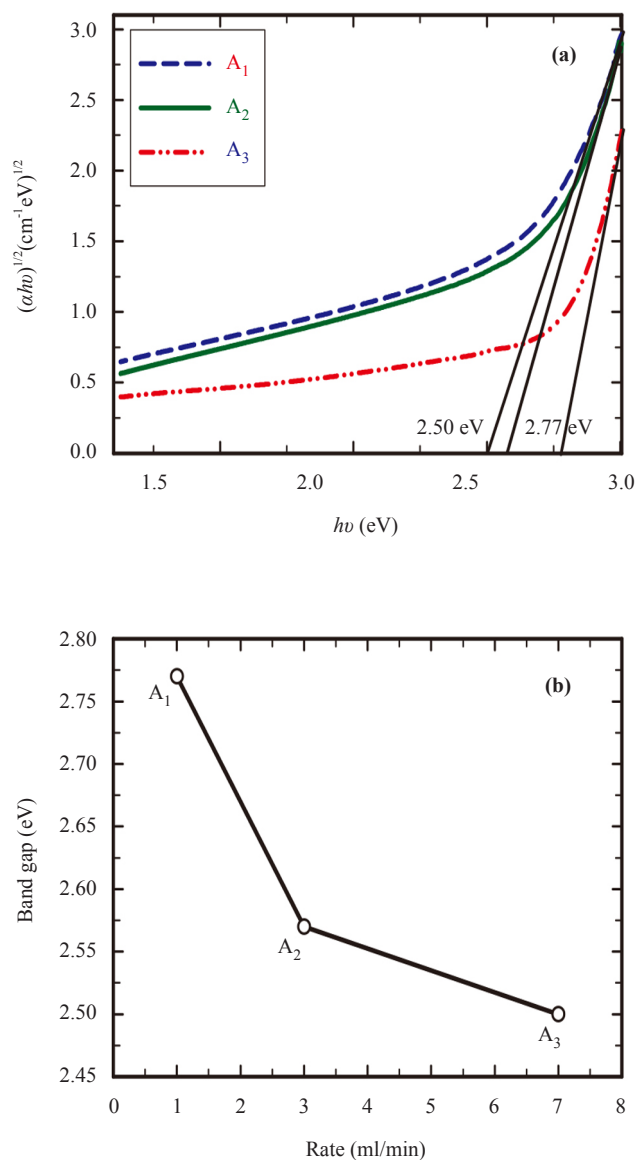

Figure 12. (a) Indirect band gaps (E_g) calculated from the absorption coefficient of the layers. The spray deposition rate influences the indirect optical band gap of the layers. (b) Comparison of the indirect band gaps (E_g) for different spray deposition rates. The optical band gap of these layers decreases with an increase in the spray deposition rate

Furthermore, our investigations reveal that the reduction in band gap mentioned earlier is related to an increase in crystal size and may be attributed to the attenuation of the quantum confinement effect [49].

4. Conclusion

In this study, we investigated the influence of the deposition rate and annealing on the physical properties of WO_3 thin films prepared by the spray pyrolysis method. The FE-SEM images revealed the formation of circular strings with varying diameters, which decreased as the deposition rate increased. The XRD analysis indicated that sample A_1 exhibited a polycrystalline structure with mixed hexagonal-tetragonal phases.

Analysis of the optical data showed a decrease in the indirect band gap of the layers from 3.51 eV to 3.11 eV, attributed to changes in the width of the band tails of oxygen vacancies defect states near the band edges.

Regarding the Seebeck effect, our experimental results indicated that sample A_1 exhibited n-type conductivity, with electrons being the majority carriers, while samples A_2 and A_3 exhibited p-type conductivity, with holes being the majority carriers. After annealing, samples A_1 and A_3 exhibited crystallization in different structures. Additionally, the annealed films displayed a relatively high absorption coefficient of approximately 10^5 cm^{-1} and an indirect transition gap within the range of 2.50-2.77 eV for samples A_1 and A_3. Furthermore, we observed that these materials exhibited n-type characteristics after annealing. Based on our analysis, we have demonstrated the potential of the Seebeck effect as a useful experimental tool for determining the conductivity type of WO_3 under different conditions. As part of our future plans, we are currently conducting electrical measurements to optimize the resistivity of these thin films.

Acknowledgements

Conflict of interest

The authors declare no competing financial interest.

References

[1] Dalavi DS, Suryavanshi MJ, Patil DS, Mali SS, Moholkar AV, Kalagi SS, et al. Nanoporous nickel oxide thin films and its improved electrochromic performance: Effect of thickness. *Applied Surface Science*. 2011; 257: 2647-2656. Available from: https://doi.org/10.1016/j.apsusc.2010.10.037.

[2] Zhang J, Wang XL, Xia XH, Gu CD, Tun JP. Electrochromic behavior of WO_3 nanotree films prepared by hydrothermal oxidation. *Solar Energy Materials & Solar Cells*. 2011; 95: 2107-2112. Available from: https://doi.org/10.1016/j.solmat.2011.03.008.

[3] Kim CY, Cho SG, Lima TY. Cycle test and degradation analysis of WO_3/PC+LiClO$_4$/CeO$_2$·TiO$_2$ electrochromic device. *Solar Energy Materials and Solar Cells*. 2009; 93(12): 2056-2061. Available from: https://doi.org/10.1016/j.solmat.2009.07.007.

[4] Rao MC. Structure and properties of 3 thin films for electrochromic device application. *Journal of Non-Oxide Glasses*. 2013; 5: 1-8.

[5] Marques A, Santos L, Pereira S, Emanuele U, Sinopoli S, Igreja R, et al. A planar electrochromic device using WO_3 nanoparticles and a modified paper-based electrolyte. *Proceedings*. 2018; 2: 1065. Available from: https://doi.org/10.3390/proceedings2131065.

[6] Qu H, Zhang X, Zhang H, Tian Y, Li N, Lv H, et al. Highly robust and flexible WO_3·2H$_2$O/PEDOT films for improved electrochromic performance in near-infrared region. *Solar Energy Materials & Solar Cells*. 2017; 163:

23-30. Available from: https://doi.org/10.1016/j.solmat.2016.12.030.

[7] Mouratis K, Tudose IV, Romanitan C, Pachiu C, Popescu M, Simistiras G, et al. WO_3 films grown by spray pyrolysis for smart windows applications. *Coatings*. 2022; 12: 545. Available from: https://doi.org/10.3390/coatings12040545.

[8] Razmi H, Rezaei RM. Preparation of tungsten oxide nanoporous thin film at carbon ceramic electrode for electrocatalytic applications. *Electrochimica Acta*. 2011; 56: 7220-7223. Availble from: https://doi.org/10.1016/j.electacta.2011.04.018.

[9] Gullapalli SK, Vemuri RS, Manciu FS, Enriquez JL, Ramana CV. Tungsten oxide (WO_3) thin films for application in advanced energy systems. *Journal of Vacuum Science and Technology A: Vacuum, Surfaces, and Films*. 2010; 28: 824-828. Available from: https://doi.org/10.1116/1.3368495.

[10] Wang Y, Ramos I, Santiago-Avil' es JJ. Optical bandgap and photoconductance of electrospun tin oxide nanofibers. *Journal of Applied Physics*. 2007; 102: 093517. Available from: https://doi.org/10.1063/1.2800261.

[11] Wang L, Zan L. WO_3 in suit embed into MIL-101 for enhancement charge carrier separation of photocatalyst. *Scientific Reports*. 2019; 9: 4860. Available from: https://doi.org/10.1038/s41598-019-41374-z.

[12] Kalhori H, Coey M, Sarsari IA, Borisov K, Porter SB, Atcheson G, et al. Oxygen vacancy in WO_3 film-based FET with ionic liquid gating. *Scientific Reports*. 2017; 7: 12253. Available from: https://doi.org/10.1038/s41598-017-12516-y.

[13] Ning S, Huberman SC, Ding Z, Nahm HH, Kim YH, Kim HS, et al. Anomalous defect dependence of thermal conductivity in epitaxial WO_3 thin films. *Advanced Materials*. 2019; 31: 1903738. Available from: https://doi.org/10.1002/adma.201903738.

[14] Linhe S, Renzhi W, Sun L, Zhang X-G, Lin Y-M, Zhang KHL, et al. Direct Z-scheme WO_{3-x} nanowire-bridged TiO_2 nanorod arrays for highly efficient photoelectrochemical overall water splitting. *Journal of Energy Chemistry*. 2021; 59: 721-729. Available from: https://doi.org/10.1016/j.jechem.2020.12.010.

[15] Guangwei Z, Jinshu W, Guannan Z, Haibing C, Chen L, Hongyi L, et al. Sandwich structured WO_3 nanoplatelets for highly efficient photoelectrochemical water splitting. *Journal of Materials Chemistry A*. 2019; 7: 26077-26088. Available from: https://doi.org/10.1039/C9TA09188B.

[16] Yao L, Jing Z, Fangfang W, Xuebing C, Zhaochi F, Can L. K_2SO_4-assisted hexagonal/monoclinic WO_3 phase junction for efficient photocatalytic degradation of RhB. *ACS Applied Energy Materials*. 2018; 1: 2067-2077. Available from: https://doi.org/10.1021/acsaem.8b00168.

[17] Sivathas SS, Murugan S, Babu AV, Ramalingam S, Thirumurugan R, Victoria DCERB. Characterization of WO_3 thin films deposited by spray pyrolysis technique and its role in gas sensing EUREKA. *Physics and Engineering*. 2022; 4: 101-113. Available from: https://doi.org/10.21303/2461-4262.2022.002347.

[18] Lu R, Zhong X, Shang S, Wang S, Tang M. Effects of sintering temperature on sensing properties of WO_3 and Ag-WO_3 electrode for NO_2 sensor. *Royal Society Open Science*. 2018; 5: 171691. Available from: https://doi.org/10.1098/rsos.171691.

[19] Heieh YT, Huang MW, Chang CC, Chen US, Shih HC. Growth and optical properties of uniform tungsten oxide nanowire bundles via a two-step heating process by thermal evaporation. *Thin Solid Films*. 2010; 519: 1668-1672. Available from:https://doi.org/10.1016/j.tsf.2010.08.162.

[20] Cole B, Marsen B, Miller E, Yan Y, To B, Jones K, et al. Evaluation of nitrogen doping of tungsten oxide for photoelectrochemical water splitting. *Journal of Physical Chemistry C*. 2008; 112: 5213. Available from: https://doi.org/10.1021/jp077624c.

[21] Granqvist CG. Electrochromic tungsten oxide films: Review of progress 1993-1998. *Solar Energy Materials & Solar Cells*. 2000; 60: 201-262. Available from: https://doi.org/10.1016/S0927-0248(99)00088-4.

[22] Sella C, Maaza M, Nemraoui O, Lafait J, Renard N, Sampeur Y. Preparation, characterization and properties of sputtered electrochromic and thermochromic devices. *Surface & Coatings Technology*. 1998; 98: 1477-1482. Available from: https://doi.org/10.1016/S0257-8972(97)00154-0.

[23] Bertus LM, Enesca A, Duta A. Influence of spray pyrolysis deposition parameters on the optoelectronic properties of WO_3 thin films. *Thin Solid Films*. 2012; 520: 4282-4290. Available from: https://doi.org/10.1016/j.tsf.2012.02.052.

[24] Kovendhan M, Joseph DP, Kumar ES, Sendilkumar A, Manimuthu P, Sambasivam S, et al. Structural transition and blue emission in textured and highly transparent spray deposited Li doped WO_3 thin films. *App. Surf. Sci*. 2011; 257: 8127-8133. Available from: https://doi.org/10.1016/j.apsusc.2011.04.122.

[25] Lozzi L, Ottaviano L, Passacantando M, Santucci S, Cantalini C. The influence of air and vacuum thermal treatments on the NO_2 gas sensitivity of WO_3 thin films prepared by thermal evaporation. *Thin Solid Films*. 2001; 391: 224-228. Available from: https://doi.org/10.1016/S0040-6090(01)00986-5.

[26] Cantalini C, Wlodarski W, Li Y, Passacantando M, Santucci S, Comini E, et al. Investigation on the O_3 sensitivity properties of WO_3 thin films prepared by solgel, thermal evaporation and r.f. sputtering techniques. *Sensors and Actuators B: Chemical.* 2000; 64(1-3): 182-188. Available from: https://doi.org/10.1016/S0925-4005(99)00504-3.

[27] Porqueras I, Betran E. Efficiency of Li doping on electrochromic WO_3 thin films. *Thin Solid Films.* 2000; 377: 129-133. Available from: https://doi.org/10.1016/S0040-6090(00)01424-3.

[28] Livahe J, Guzman G. Aqueous precursors for electrochromic tungsten oxide hydrates. *Solid State Ionics.* 1996; 84: 205-211. Available from: https://doi.org/10.1016/0167-2738(96)00018-5.

[29] Ronnow D, Kullman D, Granqvist CG. Spectroscopic light scattering from electrochromic tungsten-oxide-based films. *J. Appl. Phys.* 1996; 80: 423-430. Available from: https://doi.org/10.1063/1.362778.

[30] Guillén C. Polycrystalline WO_{3-x} thin films obtained by reactive DC sputtering at room temperature. *Materials.* 2023; 16: 1359. Available from: https://doi.org/10.3390/ma16041359.

[31] Guillén C. Physical properties of SnO_2/WO_3 bilayers prepared by reactive DC sputtering. *Advanced Energy Conversion Materials.* 2023; 2: 29. Available from: https://doi.org/10.37256/aecm.4220232941.

[32] Wang J, Bell JM, Skryabin IL. Kinetics of charge injection in solgel deposited WO_3. *Sol. Energy Mater. Sol. Cells.* 1999; 56: 465-475. Available from: https://doi.org/10.1016/S0927-0248(98)00190-1.

[33] Regragui M, Addou M, Outzourhit A, Bernede JC, El Idrissi E, Benseddik E, et al. Preparation and characterization of pyrolytic spray deposited electrochromic tungsten trioxide films. *Thin Solid Films.* 2000; 358: 40-45. Available from: https://doi.org/10.1016/S0040-6090(99)00682-3.

[34] Regragui M, Addou M, Outzourhit A, Bernede JC, El Idrissi E, Benseddik E, et al. Electrochromic effect in WO_3 thin films prepared by spray pyrolysis. *Solar Energy Materials & Solar Cells.* 2003; 77: 341-350. Available from: https://doi.org/10.1016/S0927-0248(02)00353-7.

[35] Gajić N, Kamberović Z, Anđić Z, Trpčevská J, Plešingerova B, Korać M. Synthesis of tribological WS_2 powder from WO_3 prepared by Ultrasonic Spray Pyrolysis (USP). *Metals.* 2019; 9(3): 277. Available from: https://doi.org/10.3390/met9030277.

[36] Mohite SV, Rajpure KY. Oxidative degradation of salicylic acid by sprayed WO_3 photocatalyst. *Materials Science and Engineering B.* 2015; 200: 78-83. Available from: https://doi.org/10.1016/j.mseb.2015.06.009.

[37] Abe R, Takami H, Murakami N, Ohtani B. Pristine simple oxides as visible light driven photocatalysts: Highly efficient decomposition of organic compounds over platinum-loaded tungsten oxide. *J. Am. Chem. Soc.* 2008; 130: 7780-7781. Available from: https://doi.org/10.1021/ja800835q.

[38] Qamar M, Gondal MA, Yamani ZH. Removal of Rhodamine 6G induced by laser and catalyzed by Pt/WO_3 nanocomposite Catal. *Comm.* 2010; 11: 768-772. Available from: https://doi.org/10.1016/j.catcom.2010.02.012.

[39] Perednis D. *Thin Film Deposition by Spray Pyrolysis and the Application in Solid Oxide Fuel Cells.* ETH Zürich; 2003. Available from: https://doi.org/10.3929/ETHZ-A-004637544.

[40] Perednis D, Gauckler LJ. Thin film deposition using spray pyrolysis. *Journal of Electroceramics.* 2005; 14: 103-111. Available from: https://doi.org/10.1007/s10832-005-0870-x.

[41] Jeyadheepan K, Karthick P, Sanjeeviraja C. Development of automated spray pyrolysis setup for chemical vapour deposition like growth of thin solid films. *Journal of Instrumentation.* 2019; 14: P04002. Available from: https://doi.org/10.1088/1748-0221/14/04/P04002.

[42] Sivakumar R, Moses AER, Subramanian B, Jayachandran M, Trivedi DC, Sanjeeviraja C. Preparation and characterization of spray deposited n-type WO_3 thin films for electrochromic devices. *Materials Research Bulletin.* 2004; 39: 1479-1489. Available from: https://doi.org/10.1016/j.materresbull.2004.04.023.

[43] Prabhu N, Agilan S, Muthukumarasamy N, Senthil TS. structural and morphological analysis of aluminum (Al) doped tungsten oxide (WO_3) nanoparticles. *Int. J. ChemTech Research.* 2014; 7: 3491-3495.

[44] Williamson GK, Smallman RE. III. Dislocation densities in some annealed and cold-worked metals from measurements on the X-ray debye-scherrer spectrum. *The Philosophical Magazine: A Journal of Theoretical Experimental and Applied Physics.* 2006; 1(1): 34-46. Available from: https://doi.org/10.1080/14786435608238074.

[45] Scherrer P. Nachrichten von der Gesellschaft der Wissenschaften zu Göttingen. *Mathematisch-Physikalische Klasse.* 1918; 2: 98-100.

[46] Zhang X, Ren B, Wu X, Yan X, Sun Y, Gao H, et al. Efficient Removal of Chromium (VI) using a novel waste biomass chestnut shell-based carbon electrode by electrosorption. *ACS Omega.* 2021; 39: 25389. Available from: https://doi.org/10.1021/acsomega.1c03337.

[47] Ashcroft NW, Mermin ND. *Solid State Physics.* Cornell University, Harcourt Collage Publishers; 1976. p.24-27.

[48] Owen JF, Teegarden KJ, Shanks HR. Optical properties of the sodium-tungsten bronzes and tungsten trioxide. *Phys Rev. B.* 1978; 18: 3827. Available from: https://doi.org/10.1103/PhysRevB.18.3827.

[49] Bathe SR, Patil PS. Electrochromic characteristics of fibrous reticulated WO_3 thin films prepared by pulsed spray

pyrolysis technique. *Solar Energy Materials & Solar Cells*. 2007; 91: 1097-1101. Available from: https://doi.org/10.1016/j.solmat.2007.03.005.

[50] Dabbous S, Nasrallah T, Ouerfelli J, Boubaker K, Amlouk M, Belgacem S. Study of structural and optical properties of sprayed WO_3 thin films using enhanced characterization techniques along with the Boubaker Polynomials Expansion Scheme (BPES). *Journal of Alloys and Compounds*. 2009; 487: 286-292. Available from: https://doi.org/10.1016/j.jallcom.2009.07.103.

[51] Sun Y, Murphy CJ, Gil KR, Garcia EAR, Thornton JM, Morris NA, et al. Photoelectrochemical and structural characterization of carbon-doped WO_3 films prepared via spray pyrolysis. *Int. J. Hydr. Energ*. 2009; 34: 8476-8484. Available from: https://doi.org/10.1016/j.ijhydene.2009.08.015.

[52] Chacko S, Bushiri MJ, Vaidyan VK. Photoluminescence studies of spray pyrolytically grown nanostructured tin oxide semiconductor thin films on glass substrates. *J. of Phys. D: App. Phys*. 2006; 39: 4540. Available from: https://doi.org/10.1088/0022-3727/39/21/004.

[53] Sawaby A, Selim MS, Marzouk SY, Hosny A. Structure, optical and electrochromic properties of NiO thin films. *Physica B*. 2010; 405: 3412-3420. Available from: https://doi.org/10.1016/j.physb.2010.05.015.

[54] Dickens DG, Wittingham MS. The tungsten bronzes and related compounds. *Quart. Rev. Chem. Soc*. 1968; 22: 30-44. Available from: https://doi.org/10.1039/QR9682200030.

[55] Lightsey PA. Percolation view of transport properties in $NaxWO_3$. *Phys Rev. B*. 1973; 8: 3586. Available from: https://doi.org/10.1103/PhysRevB.8.3586.

[56] Crandall RS, Faughnan BW. Electronic transport in amorphous H_xWO_3. *Phys Rev. Lett*. 1977; 39: 232. Available from: https://doi.org/10.1103/PhysRevLett.39.232.

[57] Patila PS, Patil PR, Ennaouic EA. Characterization of ultrasonic spray pyrolyzed tungsten oxide thin films. *Thin Solid Films*. 2000; 370: 38-44. Available from: https://doi.org/10.1016/S0040-6090(00)00745-8.

[58] Gilleta M, Aguira K, Lemirea C, Gilleta E, Schierbaumb K. The structure and electrical conductivity of vacuum-annealed WO_3 thin films. *Thin Solid Films*. 2004; 467: 239-246. Available from: https://doi.org/10.1016/j.tsf.2004.04.018.

[59] Wang Y, Wang X, Xu Y, Chen T, Liu M, Niu F, et al. Simultaneous synthesis of WO_3-x quantum dots and bundle-like nanowires using a one-pot template-free solvothermal strategy and their versatile applications. *Small*. 2017; 13: 1603689. Available from: https://doi.org/10.1002/smll.201603689.